#### PHYSICAL REVIEW E 95, 063103 (2017)

## Criteria for drop generation in multiphase microfluidic devices

Joseph D. Buttacci and Michael Loewenberg\*

Department of Chemical and Environmental Engineering, Yale University, New Haven, Connecticut 06520-8286, USA

## Christine C. Roberts, Martin B. Nemer, and Rekha R. Rao

Engineering Sciences Center, Sandia National Laboratories, P.O. Box 5800, MS 0346, Albuquerque, New Mexico 87185, USA (Received 24 October 2016; revised manuscript received 11 January 2017; published 6 June 2017)

A theory is presented for the transition between the coflowing and the drop-generation regimes observed in microfluidic channels with a rectangular cross section. This transition is characterized by a critical ratio of the dispersed- to continuous-phase volume flow rates. At flow-rate ratios higher than this critical value, drop generation is suppressed. The critical ratio corresponds to the fluid cross section where the dispersed-phase fluid is just tangent to the channel walls. The transition criterion is a function of the ratio of the fluid viscosities, the three-phase contact angle formed between the fluid phases and the channel walls, and the aspect ratio of the channel cross section; the transition is independent of interfacial tension. Hysteretic behavior of drop generation with respect to the flow-rate ratio is predicted for partially wetting dispersed-phase fluids. Experimental data are consistent with this theory.

#### DOI: 10.1103/PhysRevE.95.063103

#### I. INTRODUCTION

The field of microfluidics has led to devices with lowered costs that are capable of swift analysis, yielding a high resolution and increased sensitivity [1]. Many devices for controlling microfluidic flows have been developed, the most common being T-junction [2], flow-focusing [3], and coflowing [4] devices. Some applications, such as microfluidic rheometry [5,6], rely on coflowing streams of immiscible fluids. Most applications, however, rely on precisely controlled drop generation and many mechanisms of drop generation have been identified, including squeezing, dripping, and jetting modes [7–9]; applications that rely on drop generation include high-throughput screening devices [10] and biochemical assays [11]. Controlling the transition between coflowing and drop-generation regimes is critical to the design and optimization of microfluidic devices and is the subject of this paper.

The breakup of a cylindrical fluid stream surrounded by a second coflowing immiscible fluid results from the interfacial-tension-driven growth of varicose waves at the fluid-fluid interface. The confining walls of a microfluidic device can hinder breakup [12–14], and drop generation does not occur for a fluid stream in contact with confining walls because the pinned contact lines prevent the growth of varicose waves [15,16]. The two-fluid coflowing cross-section configuration shown in Fig. 1(a) is unstable because the inner fluid stream does not span the channel, leading to drop generation. The coflowing configuration shown in Fig. 1(c) is stable due to confinement. The critical cross-section configuration that separates the drop-generation and coflowing regimes in a rectangular channel corresponds to that depicted in Fig. 1(b).

The stable configuration depicted in Fig. 1(c) corresponds to the case where the inner fluid is nonwetting. If the inner fluid partially wets the channel walls, a typical stable configuration corresponds to that depicted in Fig. 1(e). The configuration

depicted in Fig. 1(d) is a second critical configuration that arises in systems with partially wetting dispersed-phase fluids. The presence of two critical configurations [Figs. 1(b) and 1(d)] for a partially wetting dispersed-phase fluid explains the hysteretic behavior of drop generation observed in some experiments [17]. Accordingly, the critical configuration depends on whether the transition is from coflowing to drop generation or vice versa.

An analysis of critical two-phase configurations [Figs. 1(b) and 1(d)] in microfluidic devices is presented. The results provide quantitative criteria for the transition between coflowing and drop-generation regimes. The problem is formulated and the critical flow-rate ratio, corresponding to the critical configuration, is defined in Sec. II. The calculation of the critical flow-rate ratio is described in Sec. III. Analytical and numerical results are presented in Secs. IV and V, respectively, and the theory is compared to experimental data in Sec. VI.

#### II. CRITICAL FLOW-RATE RATIO

The cross-section configurations shown in Fig. 1 are characterized by a flow-rate ratio  $Q_1/Q_2$ , where  $Q_1$  and  $Q_2$  are the volume flow rates of Fluid 1 and Fluid 2, respectively. Figures 1(b) and 1(d) correspond to the critical values  $Q_1/Q_2 = (Q_1/Q_2)_{\rm Cr}$  that separate the drop-generation and coflowing regimes. The drop-generating configuration depicted in Fig. 1(a) corresponds to a subcritical value of  $Q_1/Q_2$  and the coflowing configurations depicted in Figs. 1(c) and 1(e) correspond to a supercritical  $Q_1/Q_2$ . The aim of this paper is to determine the dependence of the critical flow-rate ratio  $(Q_1/Q_2)_{\rm Cr}$  on the system parameters.

#### A. Assumptions

Under the assumption that the fluids are incompressible and the channel has a constant cross section (and the flow is laminar), the dimensionless velocity fields  $\mathbf{u}^{(i)}$  (i=1,2) are unidirectional [5,16,18], i.e.,  $\mathbf{u}^{(i)}(x,y,z) = u^{(i)}(x,y)\mathbf{e}_z$ , where the superscripts 1 and 2 refer to the dispersed and continuous

<sup>\*</sup>michael.loewenberg@yale.edu

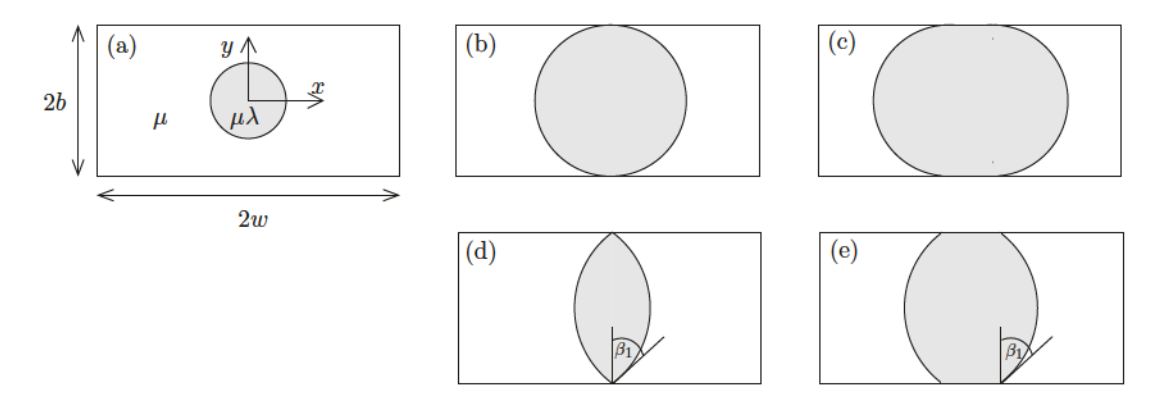


FIG. 1. Two-fluid cross-section configurations corresponding to (a) drop generation, (c, e) co-flowing, and (b, d) critical configurations in a  $2b \times 2w$  rectangular channel. The dispersed-phase (shaded) and continuous-phase viscosities,  $\mu\lambda$  and  $\mu$ , coordinate system, and three-phase contact angle  $\beta_1$  are shown. The flow is out of the page, in the +z direction.

phases (Fluid 1 and Fluid 2) and  $e_z$  is a unit vector in the z direction. Here, dimensionless variables are defined,

$$x = \frac{x_*}{b}, \quad y = \frac{y_*}{b}, \quad z = \frac{z_*}{b}, \quad u^{(i)} = \frac{\mu u_*^{(i)}}{Gb^2},$$
 (1)

where asterisks denote dimensional quantities, 2b is the channel depth as shown in Fig. 1,  $\mu$  is the viscosity of Fluid 2, and G is the pressure gradient (the same in both phases [5,16,18]). Accordingly, the velocities are governed by

$$\nabla^2 u^{(1)} = -\lambda^{-1}, \quad \nabla^2 u^{(2)} = -1, \tag{2}$$

where  $\lambda$  is the ratio of the viscosity of Fluid 1 to that of Fluid 2; steady state is assumed. Fluid 2 satisfies no-slip conditions at the channel boundaries,

$$u^{(2)} = 0$$
,  $y = \pm 1$ , or  $x = \pm W$ , (3)

where 2w is the width of the microchannel and W = w/b is the aspect ratio of the channel (cf. Fig. 1);  $W \ge 1$  is assumed. Continuity of velocity and tangential stress are enforced at the fluid interface,

$$u^{(1)} = u^{(2)}, (4a)$$

$$\lambda \frac{\partial u^{(1)}}{\partial n} = \frac{\partial u^{(2)}}{\partial n}.$$
 (4b)

Under the assumption that surface tension is sufficient to dominate normal stresses from gravity, the velocities are independent of the magnitude of interfacial tension [18] and the fluid interface is described by a circular arc with radius  $R = \csc \beta_1$  that intersects the points  $(0, \pm 1)$ , where the three-phase contact angle  $\beta_1$  is the complement of the usual contact angle. The range  $0 \le \beta_1 \le \pi/2$  is assumed.

The length of the unidirectional flow region is assumed to be sufficiently long for unstable configurations [cf. Fig. 1(a)] to undergo breakup. The velocity fields are obtained by solving Eqs. (2)–(4) and volume flow rates are calculated.

A unidirectional analysis may also be relevant for determining the transition between drop generation and coflowing operation in nonunidirectional devices. In a T-junction device, for example, two-fluid configurations similar to those shown in Fig. 1 describe the flow downstream from the actual junction, where the velocity fields are unidirectional.

According to the foregoing assumptions, the critical flowrate ratio  $(Q_1/Q_2)_{C\Gamma}$  depends on the viscosity ratio  $\lambda$ , the three-phase contact angle  $\beta_1$ , and the aspect ratio of channel W and is independent of interfacial tension.

#### III. CALCULATION OF THE FLUID VELOCITY FIELDS

The critical volume flow rates of Fluids 1 and 2 are calculated by computing the velocities and evaluating the volume flux for the critical configurations of the system [cf. Figs. 1(b) and 1(d)]. For convenience,  $Q_2$  is decomposed as

$$Q_2(\lambda, \beta_1, W) = Q_0(W) - Q_2'(\lambda, \beta_1, W), \tag{5}$$

where  $Q_0$  is the volume flow of Fluid 2 in the absence of Fluid 1 and  $Q'_2$  is the disturbance due to the presence of Fluid 1. As shown below,  $Q'_2$  decays exponentially to a form independent of W

Solutions of Eqs. (2)–(4) for the velocity fields in Fluids 1 and 2 are given by

$$u^{(1)}(x,y) = \lambda^{-1} (u_p(y) + v_1(x,y)), \tag{6}$$

$$u^{(2)}(x,y) = u_0(x,y) + v_2(x,y).$$
 (7)

The base velocity field of Fluid 2,  $u_0$ , corresponding to the flow in the absence of Fluid 1 is given by

$$u_0(x, y) = u_p(y) - u_w(x, y),$$
 (8)

where  $u_p$  is the pressure-driven component of the velocity,

$$u_p(y) = \frac{1}{2}(1 - y^2),$$
 (9)

and  $u_w$  is the wall correction that enforces boundary condition (3) at  $x = \pm W$ ,

$$u_w(x,y) = \sum_{k=0}^{\infty} d_k \frac{\cosh \alpha_k x}{\cosh \alpha_k W} \cos \alpha_k y, \tag{10}$$

$$d_k = 2(-1)^k \alpha_k^{-3},\tag{11a}$$

$$\alpha_k = (k+1/2)\pi. \tag{11b}$$

The terms  $v_1$  and  $v_2$  in Eqs. (6) and (7) are series expansions that account for hydrodynamic interactions between the fluids,

$$v_1(x,y) = \sum_{k=0}^{\infty} c_k^{(1)} f_1(x,k) g(y,k), \tag{12}$$

$$v_2(x,y) = \sum_{k=0}^{\infty} c_k^{(2)} f_2(x, W, k) g(y, k), \tag{13}$$

where

$$f_1(x,k) = \cosh \alpha_k x,\tag{14}$$

$$f_2(x, W, k) = \frac{\sinh \alpha_k (W - x)}{\sinh \alpha_k W},$$
 (15)

$$g(y,k) = \cos \alpha_k y. \tag{16}$$

According to (15) and (16),  $v_2(x,y)$ , and thus  $u^{(2)}(x,y)$ , satisfies boundary condition (3).

The coefficients  $c_k^{(i)}$  (i=1,2) are determined by truncating the velocity expansions, (6) and (7), at k=N-1 and substituting them into boundary conditions (4). A  $2N \times 2N$  system of linear equations is generated by taking the term-by-term inner product with the basis functions  $f_1(x,k)g(y,k)$  (k=0,N-1) on a quarter of the fluid interface,

$$x(s) = R\cos(s/R) - \cot\beta_1, \quad y(s) = R\sin(s/R), \quad (17)$$

$$0 \le s \le \beta_1 R$$
,  $R = \csc \beta_1$ , (18)

where  $\beta_1 R$  is the arc length of the interface over one quadrant of the cross-section configuration. The aspect-ratio dependence of the expansion coefficients  $c_k^{(i)}$  decays exponentially for  $W\gg 1$  because  $f_2\approx e^{-\alpha_k x}$  and  $u_w\approx 0$  at the fluid interface.

Formulas for evaluating the critical flow rates,  $Q_1$  and  $Q_2$ , are provided in Appendix A. For  $W \gg 1$ , the aspectratio dependence of  $Q_1$  and  $Q_2'$  decays exponentially and  $Q_0$  reduces to the linear form, (A12). Approximate results for  $W \gg 1$  are thus obtained from limiting calculations for  $W \to \infty$ .

Solutions (6) and (7) fail to converge as  $\beta_1$  and  $\lambda$  increase. However, the expansions described below for  $\beta_1 = \pi/2$  and for  $\beta_1 \ll 1$  exhibit better convergence and help to circumvent this difficulty.

#### A. Nonwetting dispersed-phase fluid, $\beta_1 = \pi/2$

The special case of the nonwetting Fluid 1 is considered here. The velocity field in Fluid 2 is described as above, but Fluid 1 is more conveniently described in cylindrical coordinates  $(r, \theta, z)$ , where r is measured from the origin and  $\theta$  is measured relative to the x axis of the Cartesian coordinate system shown in Fig. 1(a). Accordingly,

$$u^{(1)}(r,\theta) = \lambda^{-1} \left( u_p^{(1)}(r) + v_1(r,\theta) \right), \tag{19}$$

where the pressure-driven component is given by

$$u_n^{(1)}(r) = \frac{1}{4}(1 - r^2)$$
 (20)

and

$$v_1(r,\theta) = \sum_{k=0}^{\infty} c_k^{(1)} f_1(r,k) g_1(\theta,k), \tag{21}$$

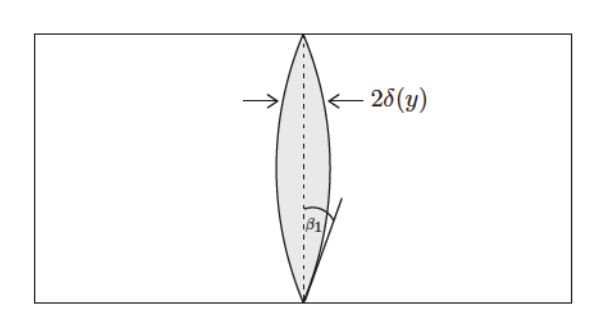


FIG. 2. Critical cross section for a partially wetting dispersedphase fluid showing the contact angle  $\beta_1$  and thickness profile  $2\delta(y)$ .

with basis functions

$$f_1(r,k) = r^{2k},$$
 (22a)

$$g_1(\theta, k) = \cos 2k\theta.$$
 (22b)

In the special case W = 1, the odd coefficients  $c_{2k+1}^{(1)}$  vanish by symmetry.

The coefficients in expansions (21) and (13) are determined by the procedure described in the previous section except, here, the basis functions used for the inner products are  $g_1(\theta, k)$ . Only the first coefficient enters the critical flow rate of Fluid 1, as given by Eq. (A5).

## B. Lubrication approximation for $\beta_1 \ll 1$

For  $\beta_1 \ll 1$ , the thickness profile of the slender lenticular region occupied by Fluid 1 (cf. Fig. 2) is given by

$$\delta(y) = \beta_1 \bar{\delta}(y) + O(\beta_1^3), \tag{23a}$$

$$\bar{\delta}(y) = \frac{1}{2}(1 - y^2).$$
 (23b)

A lubrication approximation of the velocity of Fluid 1 is appropriate provided that  $\beta_1 \ll W$  (here ensured by the assumption that  $W \geqslant 1$ ). Accordingly, the velocity of Fluid 1 is

$$u^{(1)}(x,y) = u_I(y) + u_p^{(1)}(x,y),$$
 (24)

where  $u_I(y)$  is the plug-flow component (with respect to the x direction) resulting from the velocity at the interface and  $u_p^{(1)}(x,y)$  is the pressure-driven component,

$$u_I(y) = u^{(2)}(0, y),$$
 (25a)

$$u_p^{(1)}(x,y) = \frac{1}{2\lambda} (\delta^2(y) - x^2).$$
 (25b)

Continuity of the velocity at the fluid interface is thus enforced. According to the lubrication approximation, Fluid 1 is eliminated from the problem, its influence incorporated through a modified boundary condition for Fluid 2 derived from continuity of tangential stress,

$$\frac{\partial v_2}{\partial x} + \lambda \beta_1 \frac{\partial}{\partial y} \left( \bar{\delta}(y) \frac{\partial v_2}{\partial y} \right) = \beta_1 (1 - \lambda) \frac{\partial}{\partial y} \left( \bar{\delta}(y) \frac{\partial u_0}{\partial y} \right),$$

$$x = 0.$$
(26)

The result indicates that Fluid 1 acts like a position-dependent surface viscosity,  $\lambda \beta_1 \bar{\delta}(y)$ . This boundary condition leads to a linear system of equations for the coefficients in expansion (13), as shown in Appendix C.

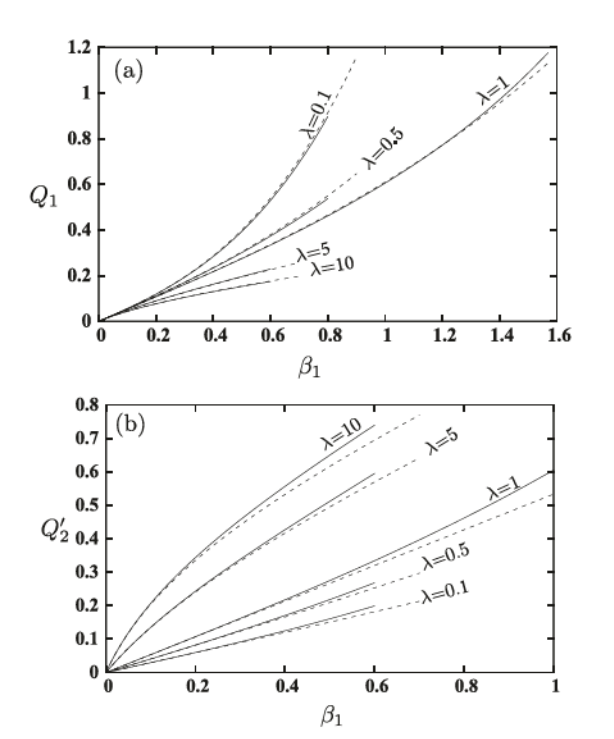


FIG. 3. Critical flow rates for the exact solution (solid lines) and lubrication approximation (dashed lines);  $W \gg 1$ .

The critical flow rate of Fluid 1 reduces to

$$Q_1(\lambda, \beta_1, W) = Q_{\text{int}} + \lambda^{-1} Q_0^{(1)},$$
 (27)

$$Q_{\text{int}} = 4\beta_1 \int_0^1 u^{(2)}(0, y) \bar{\delta}(y) \, dy, \qquad (28a)$$

$$Q_0^{(1)} = \frac{8}{105}\beta_1^3,\tag{28b}$$

where  $Q_{\text{int}}$  results from the plug-flow component of the velocity, (25a), and  $Q_0^{(1)}$  results from the pressure-driven component, (25b). The pressure-driven component is insignificant unless  $\lambda \leqslant O(\beta_1^2)$ . Formulas for  $Q_{\text{int}}$  and  $Q_2'$  are provided in Appendix C.

The results shown in Fig. 3 indicate that the flow rates obtained using the lubrication approximation agree with the converged exact solution even at moderate  $\beta_1$ . All subsequent results for  $\beta_1 < \pi/2$  were obtained using the lubrication approximation.

#### IV. ANALYSIS FOR LOW- AND HIGH-VISCOSITY RATIOS

Here, the limiting cases of low- and high-viscosity ratios are presented, considering separately the cases of a nonwetting and a wetting dispersed-phase fluid. A summary of these results is reported in Table I. The derivation of these formulas is given in the remainder of this section and in Appendixes B and C.

## A. Nonwetting dispersed-phase fluid, $\beta_1 = \pi/2$

For  $\lambda \to 0$ , the velocity field in Fluid 1 effectively satisfies no-slip boundary conditions at the fluid interface, and the velocity in Fluid 2 satisfies free-surface boundary conditions. By a regular perturbation for  $\lambda \ll 1$ , presented in Appendix B 1, the critical volume flow rates have expansions

$$Q_1(\lambda, W) = \lambda^{-1} Q_0^{(1)} + Q_1^{(1)} + O(\lambda), \tag{29}$$

$$Q_2'(\lambda, W) = Q_0^{(2)} + \lambda Q_1^{(2)} + O(\lambda^2), \tag{30}$$

where  $\mathcal{Q}_0^{(1)}=\pi/8$  and the parameters  $\mathcal{Q}_1^{(1)},\,\mathcal{Q}_0^{(2)},$  and  $\mathcal{Q}_1^{(2)}$  are plotted in Fig. 4.

In the limit  $\lambda \to \infty$ , the velocity in Fluid 2 satisfies no-slip boundary conditions at the fluid interface, yielding a disturbance flow rate that depends only on the aspect ratio at leading order. However,  $\lambda \to \infty$  is a singular limit and a boundary layer analysis is required to determine the leading-order flow rate of Fluid 1 for  $\lambda \gg 1$ ;  $O(\lambda^{-1})$  boundary layers form where the fluid interface is tangent to the channel walls. According to the analysis presented in Appendix B 2, the critical flow rates are given by

$$Q_1(\lambda, W) = \lambda^{-1} Q_{\infty}^{(1)} \left( \log \lambda - C_1^{(1)} \right) + O(\lambda^{-2} \log \lambda), \quad (31)$$

$$Q_2'(\lambda, W) = Q_{\infty}^{(2)} - \lambda^{-1} B_1^{(2)} \left(\log \lambda - C_1^{(2)}\right) + O(\lambda^{-2} \log \lambda),$$
(32)

where  $Q_{\infty}^{(1)}$ ,  $C_{1}^{(1)}$ ,  $Q_{\infty}^{(2)}$ ,  $B_{1}^{(2)}$ , and  $C_{1}^{(2)}$  are plotted in Fig. 5.

For W > 1, the fluid interface is tangent only to the horizontal channel boundaries [cf. Fig 1(b)], resulting in two boundary layer regions; for W = 1, the fluid interface has four points of tangency, generating four boundary layers. Accordingly, the parameters  $Q_{\infty}^{(1)}$ ,  $C_1^{(1)}$ ,  $B_1^{(2)}$ , and  $C_1^{(2)}$  exhibit discontinuities at W = 1, as shown in Fig. 5.

TABLE I. Summary of asymptotic formulas.

Limiting regime	$Q_1$	$Q_2'$	Parameter(s)
$\beta_1 = \pi/2$	72-1 · O(1)	2(2) 2(2)	F: 4
$\lambda \ll 1$	$\frac{\pi}{8}\lambda^{-1} + Q_1^{(1)}$	$Q_0^{(2)} + \lambda Q_1^{(2)}$	Fig. 4
$\lambda \gg 1$	$\lambda^{-1}\mathcal{Q}_{\infty}^{(1)} \left(\log \lambda - C_1^{(1)}\right)$	$Q_{\infty}^{(2)} - \lambda^{-1} B_1^{(2)} (\log \lambda - C_1^{(2)})$	Fig. 5
$\beta_1 \ll \pi/2$			
$\lambda \beta_1 \ll 1$	$\lambda^{-1}\mathcal{Q}_0^{(1)} + \left(\frac{8}{15} - F_1\right)\beta_1 + \beta_1^2(\lambda - 1)F_2$	$\frac{4}{15}\beta_1(\lambda+1) - \beta_1 F_1 + \beta_1(\lambda-1) F_3$	Eqs. (28), (C11), (C13), (C14)
$\lambda \beta_1 \gg 1$	$\lambda^{-1}ig(\mathcal{Q}_{\infty}^{(1)}\log\lambdaeta_1+C_1^{(1)}ig)$	$Q_{\infty}^{(2)} - (\lambda \beta_1)^{-1} (B_1^{(2)} \log \lambda \beta_1 + C_1^{(2)})$	Eqs. (37) and (38), Fig. 6

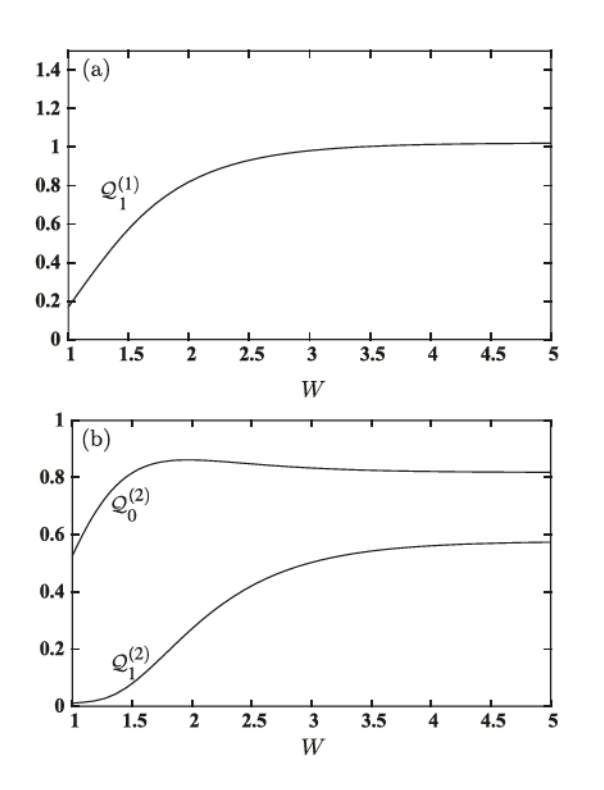


FIG. 4. Volume flow-rate coefficients for low-viscosity expansions (29) and (30).

#### B. Partially wetting dispersed-phase fluid

For  $\lambda \beta_1 \ll 1$ , the critical volume flow rate for Fluid 1 is given by Eqs. (27) and (28), where  $Q_{\text{int}}$  is

$$Q_{\text{int}} = \left(\frac{8}{15} - F_1(W)\right)\beta_1 + \beta_1^2(\lambda - 1)F_2(W), \tag{33}$$

and the critical disturbance flow of Fluid 2 is

$$Q_2' = \frac{4}{15}\beta_1(\lambda + 1) - \beta_1 F_1(W) + \beta_1(\lambda - 1)F_3(W). \tag{34}$$

Here,  $F_2(W)$  decays exponentially to a constant and  $F_1(W)$  and  $F_3(W)$  decay exponentially to 0 according to Eqs. (C11), (C13), and (C14).

The limit  $\lambda \beta_1 \to \infty$  is singular; boundary layers form near the tangent points  $(x,y)=(0,\pm 1)$  for  $\lambda \beta_1 \gg 1$ . The critical volume flow rates in this regime are given by

$$Q_1 = \lambda^{-1} (Q_{\infty}^{(1)} \log \lambda \beta_1 + C_1^{(1)}), \tag{35}$$

$$Q_2' = Q_{\infty}^{(2)} - (\lambda \beta_1)^{-1} (B_1^{(2)} \log \lambda \beta_1 + C_1^{(2)}), \qquad (36)$$

where  $Q_{\infty}^{(2)}$  is

$$Q_{\infty}^{(2)} = \frac{8}{15}\beta_1 + 8h_5 + F_4(W) - \beta_1 F_1(W), \tag{37}$$

 $h_n$  is given by Eq. (A7),  $F_4(W)$  decays exponentially to 0 and is given by (C17),  $\mathcal{Q}_{\infty}^{(1)}$  and  $B_1^{(2)}$  are

$$Q_{\infty}^{(1)} = \frac{4a_1(\beta_1, W)}{3},\tag{38a}$$

$$B_1^{(2)} = 4a_1(\beta_1, W)a_1(0, W),$$
 (38b)

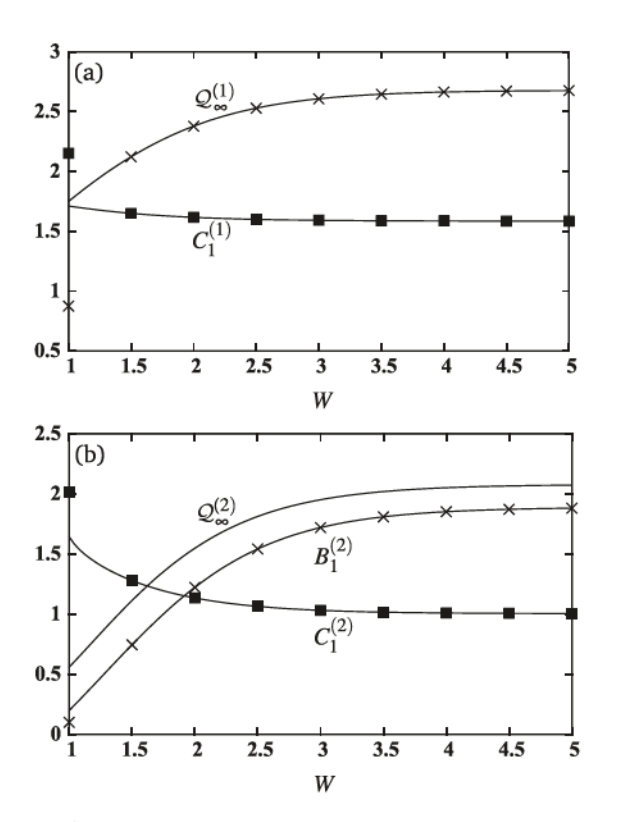


FIG. 5. Volume flow-rate coefficients for high-viscosity expansions (31) and (32). Note the discontinuities at W = 1.

and  $a_1(\beta_1, W)$  is

$$a_1(\beta_1, W) = 2\sum_{k=0}^{\infty} \alpha_k^{-3} \tanh \frac{\alpha_k W}{2} + \frac{\beta_1}{3}.$$
 (39)

The parameters  $C_1^{(1)}$  and  $C_1^{(2)}$  are obtained by extrapolating the numerical results and are shown in Fig. 6. They are approximately linear in  $\beta_1$  and almost independent of W.

## V. NUMERICAL RESULTS

Critical volume flow rates were obtained by the numerical procedure described in Sec. III. It is convenient to define the rescaled critical flow rates,

$$\Theta_1 = \frac{\lambda(Q_1 - Q_1(0, \beta_1, W))}{\mathcal{Q}_{\infty}^{(1)}} \tag{40}$$

and

$$\Theta_2 = \frac{Q_2' - Q_2'(0, \beta_1, W)}{Q_2'(\infty, \beta_1, W) - Q_2'(0, \beta_1, W)},\tag{41}$$

where  $Q_1(0,\beta_1,W)$  and  $Q_2'(0,\beta_1,W)$  correspond to the limit  $\lambda \to 0$ ,  $Q_2'(\infty,\beta_1,W)$  corresponds to  $\lambda \to \infty$ , and  $Q_{\infty}^{(1)}$  is the coefficient of  $\log \lambda$  in Eqs. (31) and (35).

The rescaled critical flow rates are shown in Fig. 7 for conditions spanning the entire ranges of the parameters W and  $\beta_1$  and a wide range of viscosity ratios. The rescaled flow rates converge exponentially in aspect ratio to the results for  $W \to \infty$ . Calculations indicate that the results are insensitive to the aspect ratio for W > 3, consistent with Figs. 4–6.

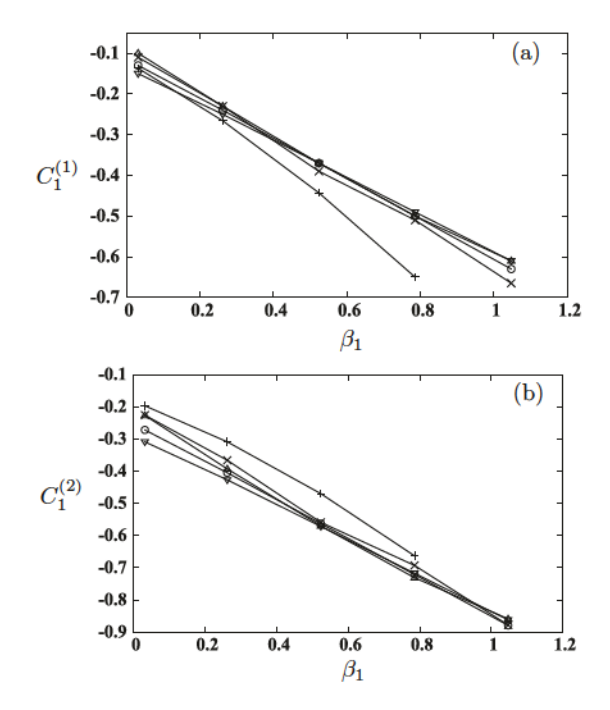


FIG. 6. Volume flow-rate coefficients for high-viscosity expansions (35) and (36) in a partially wetting system: W = 1 (crosses), W = 2 (X's), W = 3 (circles), W = 4 (upward triangles), and  $W \gg 1$  (downward triangles).

Figure 8 shows the dependence of  $(Q_1/Q_2)_{C\Gamma}$  on  $\lambda$  for W and  $\beta_1$  as indicated. The coflowing regime corresponds to  $Q_1/Q_2 > (Q_1/Q_2)_{C\Gamma}$ , i.e., Fluid 1 is confined by the channel

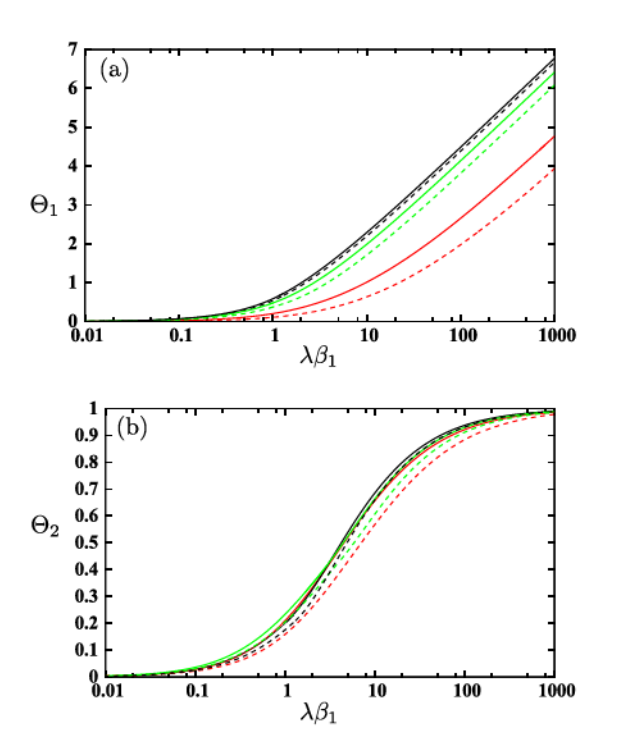


FIG. 7. Scaled critical flow rates:  $\beta_1 = \pi/2$  (red lines),  $\beta_1 = \pi/4$  (green lines),  $\beta_1 \to 0$  (black lines), W = 1 (dashed lines), and  $W \gg 1$  (solid lines).

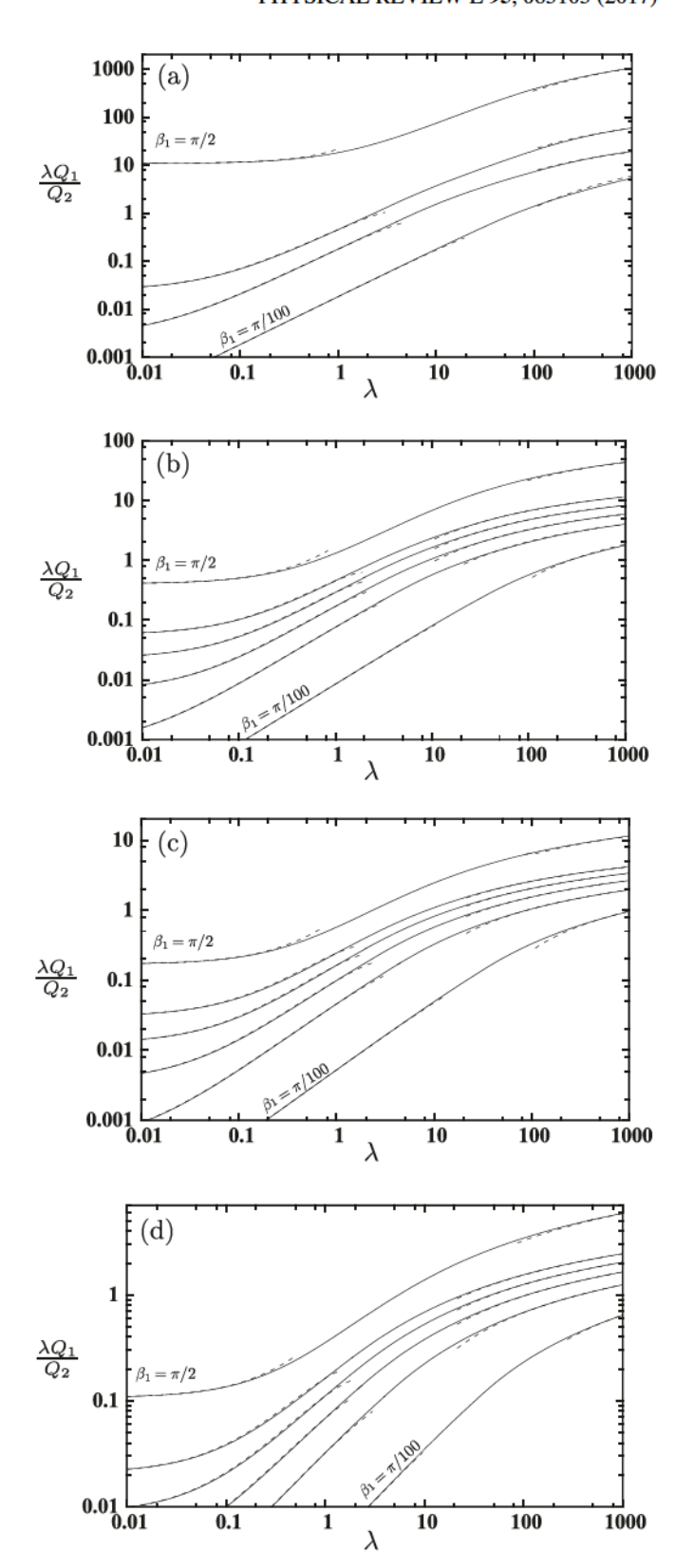


FIG. 8. Critical flow-rate ratios for (a) W=1 with (top down)  $\beta_1 = \frac{\pi}{2}, \frac{\pi}{6}, \frac{\pi}{12}$ , and  $\frac{\pi}{100}$  and for (b) W=2, (c) W=3, and (d) W=4 with (top down)  $\beta_1 = \frac{\pi}{2}, \frac{\pi}{3}, \frac{\pi}{4}, \frac{\pi}{6}, \frac{\pi}{12}$ , and  $\frac{\pi}{100}$ . Asymptotic formulas (dashed lines),  $\lambda \to 0$  and  $\lambda \to \infty$ .

walls, suppressing drop generation [cf. Figs. 1(c) and 1(e)]. Drops are generated when  $Q_1/Q_2 < (Q_1/Q_2)_{cr}$ , i.e., when Fluid 1 does not span the channel [cf. Fig. 1(a)].

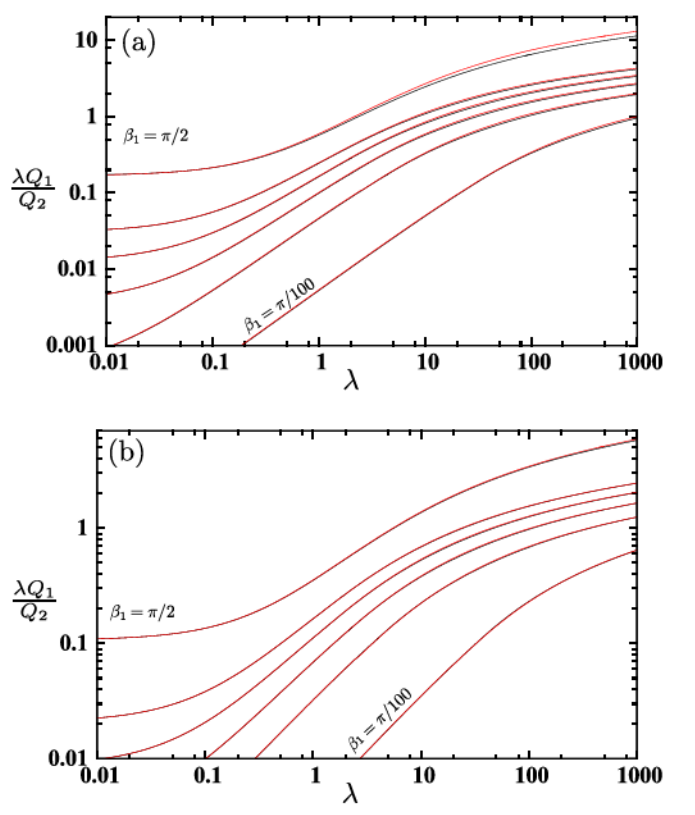


FIG. 9. Critical flow-rate ratios calculated exactly (black line) vs by the wide-channel approximation (red lines) for (a) W=3 and (b) W=4;  $\beta_1=\frac{\pi}{2},\frac{\pi}{3},\frac{\pi}{4},\frac{\pi}{6},\frac{\pi}{12}$ , and  $\frac{\pi}{100}$  (top down).

Figure 9 compares the exact calculations for  $\lambda(Q_1/Q_2)_{CT}$  with the approximate calculations for  $W\gg 1$  described in Sec. III. The results indicate that the wide-channel approximation is accurate for W>3, consistent with the insensitivity with respect to W shown in Figs. 4–7. Numerical calculations for the approximate curves shown in Fig. 9 and asymptotic formulas for low- and high-viscosity-ratios are given in Appendix D.

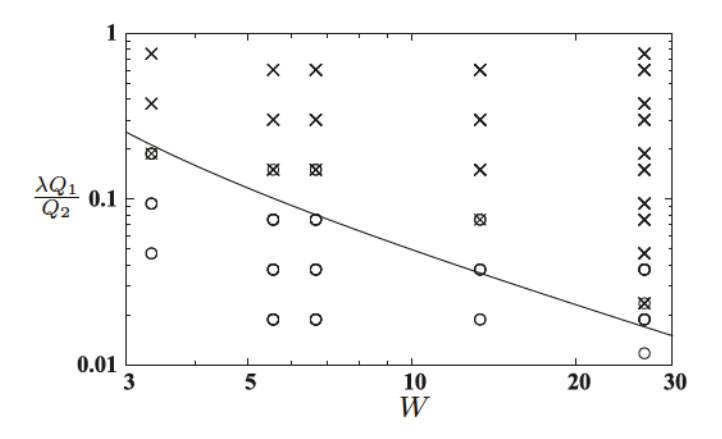


FIG. 10. Comparison of the critical flow-rate ratios predicted by theory (line) vs experiments (symbols) with the coflowing apparatus ( $\lambda = 0.19$ ,  $\beta_1 = \pi/2$ ) [15]; coflowing operation (X's) and drop generation (circles).

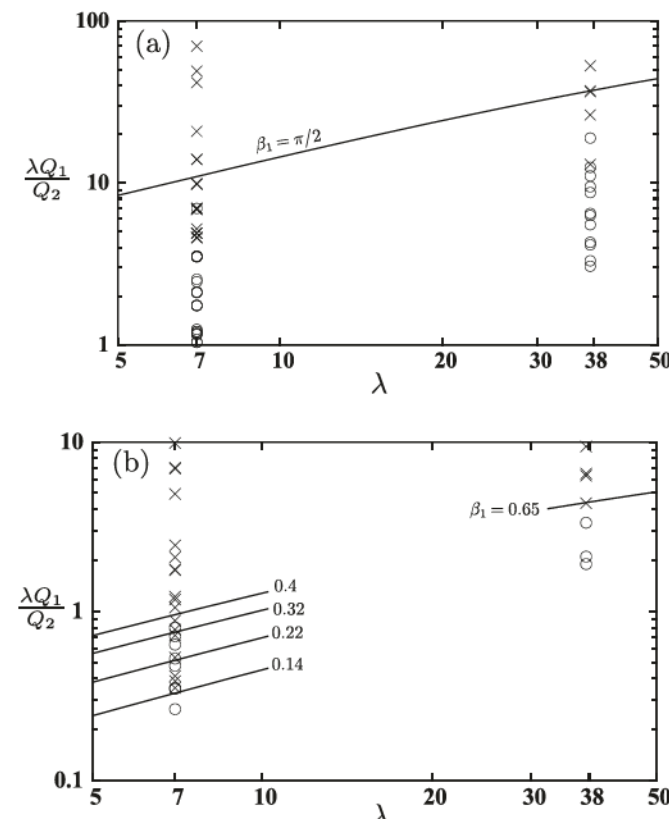


FIG. 11. Comparison of the critical flow-rate ratio predicted by theory (lines;  $\beta_1$  as indicated) vs experiments (symbols) in a T-junction apparatus (W = 1.56) [17]. (a) Transition from drop generation to coflowing and (b) transition from coflowing to drop generation; co-flowing operation (X's) and drop generation (circles).

The rescaled plots of  $Q_1$  and  $Q_2'$  shown in Fig. 7 collapse the theoretical predictions more effectively than the plots of  $\lambda Q_1/Q_2$  shown in Fig. 8. However,  $Q_2'$  is not directly measured but is instead obtained from Eq. (5). Obtaining the plots in Fig. 7 from experiments would require measurements of the pressure gradient in the region of unidirectional flow (where the critical configuration occurs) to determine the volumetric base flow  $Q_0$ . Unfortunately, the local pressure gradient is not typically reported in experiments.

For the case of the partially wetting Fluid 1, two critical cross sections are possible, as shown in Figs. 1(b) and 1(d), giving rise to hysteresis. The transition from subcritical values of  $Q_1/Q_2$  to supercritical values proceeds through the critical configuration [Fig. 1(b)] corresponding to curves with  $\beta_1 = \pi/2$  in Fig. 8; the transition from super- to subcritical values of  $Q_1/Q_2$  proceeds through the critical configuration [Fig. 1(d)] corresponding to curves with  $\beta_1 < \pi/2$  in Fig. 8. For  $\lambda \gtrsim 100$ , the results in Figs. 7 and 8 were obtained using the extrapolated  $O(\lambda^{-2})$  expansions (C27) and (C28) for  $\beta_1 < \pi/2$  and expansions (B20) and (B21) for  $\beta_1 = \pi/2$ .

The validity of the lubrication approximation relies on  $\beta_1 \ll W$  and thus fails for the largest contact angles with W=1 due to the magnification of the error caused by using the lubrication approximation for  $Q_2'$ , the exact calculation of  $Q_0$ , and the subtraction needed to obtain the flow rate of Fluid 2 according to definition (5). The results for W=1 are thus restricted to

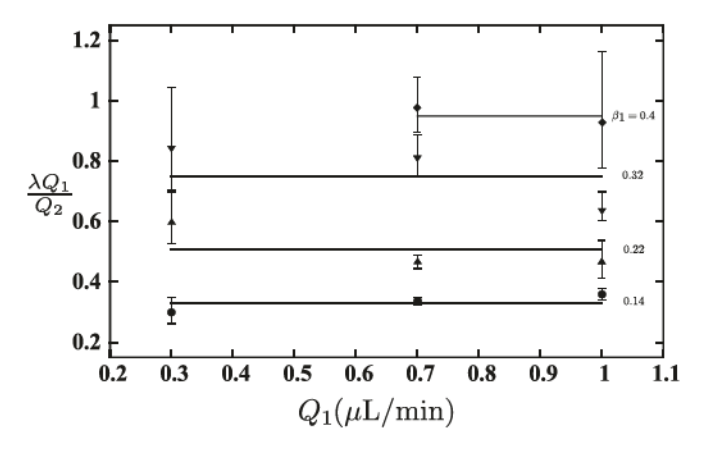


FIG. 12. Experimentally measured critical flow-rate ratios in a T-junction apparatus (W=1.56) with  $\lambda\approx 7$  for the transition from coflowing to drop generation (symbols) [17]. Surfactant in neither fluid (diamonds), surfactant in Fluid 2 (downward triangles), surfactant in Fluid 1 (upward triangles), and surfactant in both fluids (circles); theoretical predictions using best-fit contact angles as indicated (lines).

 $\beta_1 \le \pi/6$  in Fig. 8. This problem does not arise for the direct results shown in Fig. 7.

#### VI. COMPARISON WITH EXPERIMENTS

Figure 10 shows a comparison between theory and data generated by a coflowing device [15]. The figure shows that the theory is consistent with most of the observations: drops are generated for values of  $\lambda Q_1/Q_2$  below the critical curve and coflowing is observed above. Similar consistency has been observed in data from other groups [19].

Figure 11 shows a comparison between theory and T-junction data for a system that exhibits hysteresis [17]. The data for each viscosity ratio were obtained from experiments with surfactants present in one or the other or both fluids (four possible configurations). The data were provided in aggregate, distinguished only by viscosity ratio, and not surfactant configuration; contact angles were estimated from the data in Fig. 12. Comparison of Figs. 11(a) and 11(b)

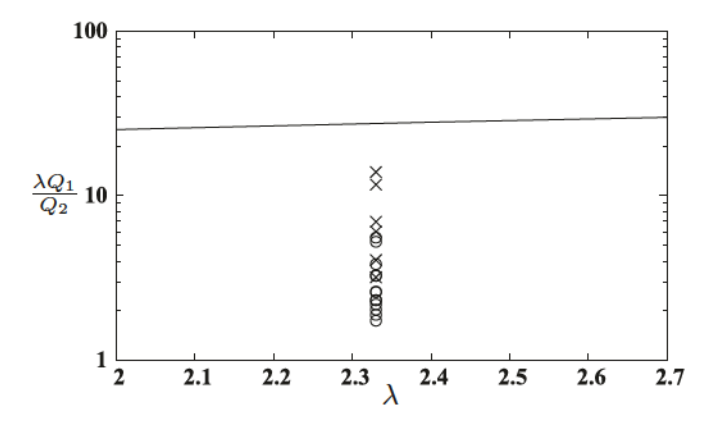
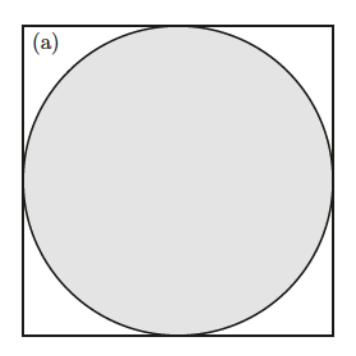


FIG. 13. Comparison of critical flow-rate ratios predicted by theory (line) vs experiments (symbols) with the T-junction apparatus (W = 1)[18]; coflowing operation (X's) and drop generation (circles).



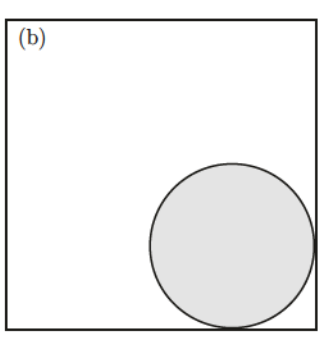


FIG. 14. Cross-section configurations for microfluidic channels with W=1 and  $\beta_1=\pi/2$ ; (a) critical configuration and (b) stable subcritical configuration.

indicates that the transition from drop generation to coflowing occurs for flow-rate ratios at least an order of magnitude higher than for the reverse transition (coflowing to drop generation).

Figure 12 shows experimentally measured critical flow-rate ratios for the transition from coflowing to drop generation [17] and theoretical predictions based on a best fit for the contact angle. Four contact angles are shown, corresponding to the four configurations of surfactants. This figure indicates that the transition from coflowing to drop generation is independent of  $Q_1$ , indicating that the transition is independent of surface tension. Data for the reverse transition from drop generation to coflowing [17] (not shown) is also insensitive to  $Q_1$ .

Figure 13 presents T-junction data for a channel with a square cross section (W=1) [18]. The transition between drop generation and coflowing occurs at a considerably lower flow-rate ratio than predicted by theory. This observation may be explained by the contrast between the predicted critical configuration for a nonwetting fluid in a square channel [cf. Fig. 14(a)] and stable subcritical coflowing configurations [cf. Fig. 14(b)] similar to those observed by Guillot and Colin [18]. Subcritical transition in square cross-section channels was also found in data from other groups [20,21]. For  $W \approx 1$ , the theory predicts only an upper bound, i.e., drop generation cannot occur for  $Q_1/Q_2 > (Q_1/Q_2)_{\rm cr}$ , but the transition may occur at lower values of  $Q_1/Q_2$ .

The transition between drop generation and coflowing operation may also occur at flow-rate ratios lower than predicted for W>1 if the stream of dispersed-phase fluid is off-center, in contrast to the assumption herein (cf. Fig. 1). In this case, the theory provides an upper bound for the transition. An off-center dispersed-phase stream may explain the subcritical coflowing shown in Fig. 11(a). Similarly, the best-fit contact angles in Fig. 12 may be underestimated.

## VII. CONCLUSIONS

An analysis of the critical flow-rate ratio for the transition between the coflowing and the drop-generation regimes is presented for microfluidic channels with a rectangular cross section. The critical flow-rate ratio corresponds to a critical two-phase flow configuration that occurs in a region of unidirectional flow (elsewhere, the velocity field may be nonunidirectional). The critical flow-rate ratio depends on the viscosity ratio of the fluids, the three-phase contact angle

formed between the fluids and the channel walls, and the aspect ratio of the channel cross section. The transition is independent of the magnitude of interfacial tension and thus is not usefully characterized by a capillary number. Hysteresis is predicted for a dispersed-phase fluid which partially wets the channel walls.

For the most part, experimental observations are consistent with the transition predicted by theory. Possible exceptions include square channels and systems with an off-center stream of dispersed-phase fluid. In these cases, the theory provides an upper bound for the transition. It should be possible to extend the unidirectional theory to these cases.

While hysteresis has been observed in microfluidic systems [19,22], Zagnoni *et al.* [17] are the first to report data in terms of the direction of the transition, i.e., from sub- to supercritical flow-rate ratio  $(Q_1/Q_2)$ , and vice versa, which is useful for interpreting hysteretic data. Measurements of the pressure drop across the region where the critical configuration occurs would allow a significant collapse of the data in terms of rescaled critical flow rates, (40) and (41), as shown in Fig. 7. Further validation of the theory will require additional experiments with partially wetting systems, including observations of the transition from coflowing to drop generation, and vice versa, as well as contact angle measurements.

#### ACKNOWLEDGMENTS

The authors wish to thank Dr. M. Zagnoni, Dr. K. Humphry, Dr. S. Vanapalli, and M. Nekouei for their assistance in comparing their experimental data to this theory. The authors are grateful for useful feedback from G. Kaufman. J.B. was supported by NSF CBET Grant No. 1603806.

#### APPENDIX A: CRITICAL VOLUME FLOW RATES

Critical volume flow rates are calculated by computing the area integrals of the velocity fields  $u^{(1)}$  and  $u^{(2)}$ , generating  $Q_1$  and  $Q_2$ . In general,  $Q_1$  is expressed as

$$Q_1(\lambda, \beta_1, W) = \lambda^{-1}(Q_{\beta} + Q_1'),$$
 (A1)

where  $Q_{\beta}$  and  $Q'_{1}$  are given by

$$Q_{\beta} = \frac{1}{24} (6R^2 \beta_1 (4 - R^2) + (6R^2 - 20) \cot \beta_1),$$
 (A2)

$$Q_1' = 4\sum_{k=0}^{\infty} c_k^{(1)} \alpha_k^{-2} (I_k^+ - I_k^-), \tag{A3}$$

and  $I_k^{\pm}$  are integrals

$$I_k^{\pm} = \frac{\alpha_k}{2} \int_0^{\beta_1 R} e^{\pm \alpha_k x(s)} \cos(\alpha_k y(s)) \frac{dy}{ds} ds. \tag{A4}$$

Here, R, x(s), and y(s) are given by (17) and (18) and  $\alpha_k$  is given by (11b). For  $\beta_1 = \pi/2$ , the volume flow rate of Fluid 1, obtained from expansion (19), is

$$Q_1(\lambda, W) = \frac{\pi}{\lambda} (\frac{1}{8} + c_0^{(1)}).$$
 (A5)

The volume flow rate of Fluid 2 is given by Eq. (5). The base flow component is the integral of the base velocity over the rectangular cross section and is given by

$$Q_0(W) = \frac{4}{3}W - 8h_5 - \left[8\sum_{k=0}^{\infty} \alpha_k^{-5}(\tanh \alpha_k W - 1)\right], \text{ (A6)}$$

where  $h_n$  is defined by

$$h_n = (2^n - 1)\pi^{-n}\zeta(n), \quad \zeta(n) = \sum_{k=1}^{\infty} k^{-n}.$$
 (A7)

The disturbance flow rate is given by

$$Q_2'(\lambda, \beta_1, W) = 4 \int_0^1 \int_0^{x(s)} u_0(x, y) \, dx \, dy(s)$$
$$-4 \int_0^1 \int_{x(s)}^W v_2(x, y) \, dx \, dy(s), \quad (A8)$$

which can be rewritten as

$$Q_2'(\lambda, \beta_1, W) = Q_\infty' + Q_W', \tag{A9}$$

and components  $Q'_{\infty}$  and  $Q'_{W}$  are given by

$$Q'_{\infty} = Q_{\beta} - 8 \sum_{k=0}^{\infty} c_k^{(2)} \alpha_k^{-2} I_k^{-}$$
 (A10)

and

$$Q'_{W} = 4 \sum_{k=0}^{\infty} c_{k}^{(2)} \alpha_{k}^{-2} (-1)^{k} \operatorname{csch} \alpha_{k} W$$

$$-4 \sum_{k=0}^{\infty} c_{k}^{(2)} \alpha_{k}^{-2} (\operatorname{coth} \alpha_{k} W - 1) (I_{k}^{+} + I_{k}^{-})$$

$$-4 \sum_{k=0}^{\infty} d_{k} \alpha_{k}^{-2} (I_{k}^{+} - I_{k}^{-}) \operatorname{sech} \alpha_{k} W. \tag{A11}$$

Coefficients  $d_k$  are given by Eq. (11a).

The aspect-ratio dependence of the expansion coefficients  $c_k^{(i)}$  (i=1,2) decays exponentially for  $W\gg 1$ , as discussed in Sec. III. Consequently,  $Q_1$  and  $Q_\infty'$  become independent of W and  $Q_W'\to 0$ . For  $W\gg 1$ , the base flow, (A6), decays exponentially to

$$Q_0(W) = \frac{4}{3}W - 8h_5. \tag{A12}$$

# APPENDIX B: LIMITING BEHAVIOR FOR A NONWETTING DISPERSED-PHASE FLUID

The behavior of a system with a nonwetting dispersed-phase fluid in the limits of  $\lambda \ll 1$  and  $\lambda \gg 1$  is analyzed here.

#### 1. Low-viscosity ratios

A regular perturbation is developed for  $\lambda \ll 1$  by expanding the velocities  $u^{(1)}$  and  $u^{(2)}$  about  $\lambda = 0$ ,

$$u^{(1)} = \lambda^{-1} u_0^{(1)} + u_1^{(1)} + \lambda u_2^{(1)} + \dots$$
 (B1)

$$u^{(2)} = u_0^{(2)} + \lambda u_1^{(2)} + \lambda^2 u_2^{(2)} + \dots$$
 (B2)

Inserting these expansions into Eqs. (2)–(4) yields

$$\nabla^2 u_j^{(i)} = \begin{cases} -1, & j = 0, \\ 0, & j > 0, \end{cases} \quad i = 1, 2,$$
 (B3)

$$u_i^{(2)} = 0$$
,  $y = \pm 1$ , or  $x = \pm W$ , (B4)

$$u_j^{(1)} = u_{j-1}^{(2)},$$
 (B5a)

$$\frac{\partial u_j^{(1)}}{\partial n} = \frac{\partial u_j^{(2)}}{\partial n}.$$
 (B5b)

The leading-order terms  $u_0^{(i)}$  are given by (19) and (7); higher-order terms are given by (21) and (13). These expansions are solved sequentially at each order j, solving first for  $u_j^{(1)}$  using boundary condition (B5a) and then for  $u_j^{(2)}$  using (B5b); the sequence is started using  $u_0^{(1)} = u_p^{(1)}(r)$ , given by (20). Integrating the velocity fields yields the critical flow rates, (29) and (30).

## 2. High-viscosity ratios

For  $\lambda \gg 1$ , the leading-order velocity in Fluid 2 satisfies no-slip boundary conditions at the fluid interface. Integrating the resulting velocity field over the cross section of Fluid 2 yields  $\mathcal{Q}_{\infty}^{(2)}$  in Eq. (32).

The net force exerted on the fluid interface by the stresses in Fluid 2 has the form

$$\mathcal{F}^{(2)} = \mathcal{F}_p + a_0(W), \tag{B6}$$

where  $\mathcal{F}_p = -\pi$ , resulting from the pressure-driven component of the velocity, (9), balances the net pressure force on Fluid 1, which is built into the expansion, (19), for  $u^{(1)}$ ; however, the additional contribution  $a_0(W)$  cannot be balanced by the stresses associated with this expansion. The force balance is achieved through the augmented expansion,

$$u^{(1)}(r,\theta) = \lambda^{-1} \left( u_p^{(1)}(r) + v_1(r,\theta) + \frac{a_0(W)}{N\pi} \sum_{i=1}^N \log r_i \right),$$
(B7)

which satisfies Eq. (2). Here,  $u_p^{(1)}$  and  $v_1$  are given by (20) and (21),  $r_i$  is the distance from a position  $(r,\theta)$  to a point of tangency between the fluid interface and the channel wall, and N is the number of tangent points. For W > 1, there are two tangent points, located at  $(r,\theta) = (1, \pm \pi/2)$ ; for W = 1, there are two additional points of tangency, at (1,0) and  $(1,\pi)$ .

Boundary layers form at the points where the fluid interface is tangent to the channel walls; expansion (B7) describes the fluid velocity in the outer region away from these boundary layers. For k > 0, the coefficients  $c_k^{(1)}$  in expansion (B7) are obtained from boundary condition (4b) using the leading-order velocity field in Fluid 2. The constant  $c_0^{(1)}$  is obtained by matching to the velocity field in the boundary layers.

## a. Boundary layer

In the boundary layer, a local Cartesian coordinate system (x', y') is defined with unit vectors  $\mathbf{e}_{x'}$  and  $\mathbf{e}_{y'}$ , where  $\mathbf{e}_{x'}$  is tangent to the fluid interface,  $\mathbf{e}_{y'}$  is normal to the interface and directed into Fluid 1, and (0,0) is the point where the

fluid interface is tangent to the wall (corresponding to  $r_i = 0$ ). In the boundary layer, Fluid 2 undergoes shear flow, and by continuity of the velocity at the interface, (4a),

$$u^{(2)}(x',y') = u^{(1)}(x',0)\left(1 + \frac{y'}{h(x')}\right),$$
 (B8)

where  $h(x') = \frac{1}{2}x'^2$  is the thickness profile of Fluid 2 in the boundary layer. The velocity satisfies no-slip conditions on the channel walls [y' = -h(x')]. Then, by boundary condition (4b),

$$\lambda \frac{\partial u^{(1)}}{\partial v'} = \frac{2u^{(1)}}{x^{2}} \tag{B9}$$

at the interface, y' = 0. Balancing this boundary condition for  $\lambda \to \infty$  requires the rescaled inner variables,

$$\tilde{x} = \lambda x', \quad \tilde{y} = \lambda y', \quad \tilde{u}^{(1)} = u^{(1)},$$
 (B10)

indicating an  $O(\lambda^{-1})$  boundary layer thickness. Inserting these variables into Eqs. (2) and (B9) yields the leading-order problem for the boundary layer velocity in Fluid 1:

$$\nabla^2 \tilde{u}^{(1)} = 0, \tag{B11}$$

$$\frac{\partial \tilde{u}^{(1)}}{\partial \tilde{v}} = \frac{2\tilde{u}^{(1)}}{\tilde{x}^2}, \quad \tilde{y} = 0.$$
 (B12)

Additionally, the boundary layer velocity is required to match the outer expansion, (B7),

$$\lim_{\tilde{r}\to\infty}\tilde{u}^{(1)}\iff \lim_{r_i\to 0}u^{(1)},\tag{B13}$$

and thus,

$$\lim \tilde{u}^{(1)} \sim \log \tilde{r}, \quad \tilde{r} \to \infty,$$
 (B14)

where  $\tilde{r} = (\tilde{x}^2 + \tilde{y}^2)^{1/2}$ .

The far-field solution of Eqs. (B11), (B12), and (B14) is

$$\lim \tilde{u}^{(1)} = \frac{a_0(W)}{N\pi\lambda} (\log \tilde{r} - \gamma - \log 2), \quad \tilde{r} \to \infty, \quad (B15)$$

where  $\gamma$  is Euler's constant. Finally, the remaining constant in expansion (B7) is obtained from the matching condition, (B13),

$$c_0^{(1)} = -\sum_{k=1}^{\infty} c_k^{(1)} (-1)^k -\frac{a_0(W)}{N\pi} \left( \left( \frac{N}{2} + 1 \right) \log 2 + \gamma - \log \lambda \right).$$
 (B16)

Here, N=2, corresponding to W>1 with tangent points at  $(r,\theta)=(1,\pm\pi/2)$ , or N=4, corresponding to the case W=1, which has additional tangent points (1,0) and  $(1,\pi)$ .

## b. Correction to the velocity in Fluid 2

Away from the boundary layer, the velocity in Fluid 2 has the form

$$u^{(2)} = u_0^{(2)} + \lambda^{-1} u_1^{(2)} + O(\lambda^{-2}),$$
 (B17)

where  $u_0^{(2)}$  is the leading-order velocity in Fluid 2 described above. The first-order correction,  $u_1^{(2)}$ , satisfies Laplace's equation and has an expansion of the form (13) with coefficients

obtained from boundary conditions

$$u_1^{(2)} = u^{(1)} \tag{B18}$$

at the fluid interface, where  $u^{(1)}$  is the leading-order velocity field in Fluid 1 given above by (B7).

#### c. Critical volume flow rates

Integrating velocity fields (B7) and (B17) yields the critical volume flow rates, (31) and (32), where the parameters  $Q_{\infty}^{(1)}$  and  $C_{1}^{(1)}$  are given by

$$Q_{\infty}^{(1)} = \frac{a_0(W)}{N}, \quad C_1^{(1)} = \log \lambda - \frac{N\pi}{a_0(W)} \left(c_0^{(1)} + \frac{1}{8}\right).$$
 (B19)

Although the boundary layer is needed to determine the velocity fields in the outer regions of Fluid 1 and Fluid 2, the direct contribution of the boundary layer velocities to the volume flow rates is negligible to the order given.

The foregoing expansions were assumed to have the extended forms

$$Q_1 = \lambda^{-1} \mathcal{Q}_{\infty}^{(1)} \left( \log \lambda - C_1^{(1)} \right) + \lambda^{-2} B_2^{(1)} \left( \log \lambda + C_2^{(1)} \right),$$
(B20)

$$Q_2' = Q_{\infty}^{(2)} + \lambda^{-1} B_1^{(2)} (\log \lambda + C_1^{(2)}) + \lambda^{-2} B_2^{(2)} (\log \lambda + C_2^{(2)}),$$
(B21)

where  $\mathcal{Q}_{\infty}^{(1)}$ ,  $C_1^{(1)}$ ,  $\mathcal{Q}_{\infty}^{(2)}$ ,  $B_1^{(2)}$ , and  $C_1^{(2)}$  correspond to Eqs. (31) and (32) and the  $O(\lambda^{-2})$  terms were obtain by numerical extrapolation. All coefficients in these expansions depend on W.

#### APPENDIX C: LUBRICATION ANALYSIS, $\beta_1 \ll 1$

Here, an analysis is presented for  $\beta_1 \ll 1$ . Under the assumption that  $\lambda \beta_1 = O(1)$ , the results are uniformly valid in  $\lambda$ . Lubrication approximations are used for the velocity of Fluid 1, (24) and (25), and the shape of the region it occupies (23) (cf. Fig. 2). As discussed in Sec. III B, the lubrication approximation automatically enforces continuity of velocity at the fluid interface.

The tangential stress exerted at the fluid interface by Fluid 2 is given by

$$\frac{\partial u^{(2)}}{\partial n} \approx \frac{\partial u^{(2)}}{\partial x} - \beta_1 \frac{d\bar{\delta}}{dy} \frac{\partial u^{(2)}}{\partial y},\tag{C1}$$

where  $\bar{\delta}(y)$  is the thickness profile, (23b), of Fluid 1. The tangential stress exerted at the fluid interface by Fluid 1, obtained from the lubrication form, (24), is given by

$$\lambda \frac{\partial u^{(1)}}{\partial n} \approx -\lambda \beta_1 \frac{\partial}{\partial y} \left( \bar{\delta}(y) \frac{\partial u^{(2)}}{\partial y} \right) - \beta_1 \bar{\delta}(y). \tag{C2}$$

Evaluating Eqs. (C1) and (C2) at x = 0 and inserting them into the tangential stress balance, (4b), yields

$$\frac{\partial u^{(2)}}{\partial x} - \beta_1 \frac{d\bar{\delta}}{dy} \frac{\partial u^{(2)}}{\partial y} = -\lambda \beta_1 \frac{\partial}{\partial y} \left( \bar{\delta}(y) \frac{\partial u^{(2)}}{\partial y} \right) - \beta_1 \bar{\delta}(y),$$

$$x = 0.$$
(C3)

Boundary condition (26) is obtained by inserting expansion (7) into this result.

Taking the inner product of Eq. (26) with  $\cos \alpha_k y$  over the interval -1 < y < 1 yields the linear system for determining the coefficients  $c_k^{(2)}$ ,

$$\mathbf{A} \cdot \mathbf{c} = \beta_1 (\lambda - 1) \mathbf{b},\tag{C4}$$

where

$$A_{ik} = \coth(\alpha_i W) \delta_{ik} + \lambda \beta_1 \alpha_k M_{ik}, \tag{C5}$$

$$b_j = 2(-1)^j (\alpha_i^{-2} - 3\alpha_i^{-4}) + w_j(W),$$
 (C6)

and  $\alpha_k$  are the eigenvalues, (11b). Here, the matrix  $M_{jk}$  is given by

$$M_{jk} = \begin{cases} -2(-1)^{j+k} \frac{\alpha_j^2 + \alpha_k^2}{\left(\alpha_j^2 - \alpha_k^2\right)^2}, & j \neq k, \\ \frac{1}{3} - \frac{1}{4\alpha_j^2}, & j = k, \end{cases}$$
(C7)

and  $w_i$  is the forcing due to the wall-correction velocity (10),

$$w_j(W) = 2\sum_{k=0}^{\infty} (-1)^k \alpha_k^{-2} \operatorname{sech}(\alpha_k W) M_{jk}.$$
 (C8)

The flow rate  $Q_1$  is given by Eq. (27). The plug-flow contribution to the volume flow rate of Fluid 1 is obtained by inserting the velocity, (7), into Eq. (28a),

$$Q_{\text{int}} = \beta_1 \left( \frac{8}{15} + 4 \sum_{k=0}^{\infty} c_k^{(2)} (-1)^k \alpha_k^{-3} - F_1(W) \right).$$
 (C9)

This formula is also obtained from Eqs. (A1)–(A3) for  $\beta_1 \ll 1$ ; formulas (A8)–(A11) yield

$$Q_2' = \frac{8}{15}\beta_1 - 4\sum_{k=0}^{\infty} c_k^{(2)} (-1)^k \alpha_k^{-2} - \beta_1 F_1(W)$$
$$-4\sum_{k=0}^{\infty} c_k^{(2)} (-1)^k \alpha_k^{-2} \left( \tanh\left(\frac{\alpha_k W}{2}\right) - 1 \right), \text{ (C10)}$$

where the term in large parentheses decays exponentially in W. The function  $F_1(W)$  is defined by

$$F_1(W) = 8 \sum_{k=0}^{\infty} \alpha_k^{-6} \operatorname{sech} \alpha_k W,$$
 (C11)

which decays exponentially to 0.

## 1. Limiting case $\lambda \beta_1 \ll 1$

For  $\lambda \beta_1 \ll 1$ , matrix A, defined by (C5), becomes diagonal, yielding

$$c_k^{(2)} = \beta_1(\lambda - 1)b_k \tanh \alpha_k W, \tag{C12}$$

where  $b_k$  is defined by Eq. (C6). Inserting this result into (C9) and (C10) yields critical volume flow rates (33) and (34), where

 $F_2$  and  $F_3$  are defined by

$$F_2(W) = 8(h_5 - 3h_7) + 8\sum_{k=0}^{\infty} (\alpha_k^{-3} - 3\alpha_k^{-5}) (\tanh \alpha_k W - 1)$$

$$+4\sum_{k=0}^{\infty}(-1)^{k}\alpha_{k}^{-3}w_{k}(W)\tanh\alpha_{k}W$$
 (C13)

and

$$F_3(W) = -8 \sum_{k=0}^{\infty} \left( \alpha_k^{-4} - 3\alpha_k^{-6} \right) \left[ \tanh\left(\frac{\alpha_k W}{2}\right) \tanh \alpha_k W - 1 \right]$$
$$-4 \sum_{k=0}^{\infty} (-1)^k \alpha_k^{-2} w_k(W) \tanh\left(\frac{\alpha_k W}{2}\right) \tanh \alpha_k W,$$
(C14)

and  $w_k(W)$  is defined by Eq. (C8). Accordingly,  $F_2$  decays exponentially to the constant  $8(h_5 - 3h_7)$ , where  $h_n$  is given by Eq. (A7), and  $F_3$  decays exponentially to 0.

#### 2. Limiting case $\lambda \beta_1 \gg 1$

For  $\lambda \beta_1 \gg 1$ , boundary condition (26) reduces to the no-slip condition,

$$u^{(2)} = 0, \quad x = 0.$$
 (C15)

The resulting velocity is given by expansion (7) with coefficients

$$c_k^{(2)} = -d_k(1 - \operatorname{sech} \alpha_k W)$$
. (C16)

Substituting these coefficients into (C10) yields Eq. (37), where

$$\begin{split} F_4(W) &= 8 \sum_{k=0}^{\infty} \alpha_k^{-5} \tanh \left( \frac{\alpha_k W}{2} \right) \\ &\times \left( 1 - \coth \left( \frac{\alpha_k W}{2} \right) - \operatorname{sech} \alpha_k W \right) \end{split} \tag{C17}$$

decays exponentially to 0.

Due to the no-slip boundary condition, (C15), the critical flow rate of Fluid 1 vanishes according to Eqs. (27) and (28). The leading-order nonzero critical flow rate of Fluid 1 is obtained by expanding the velocity of Fluid 2 for  $\lambda \beta_1 \gg 1$ ,

$$u^{(2)} = u_0^{(2)} + \Lambda^{-1} u_1^{(2)} + \Lambda^{-2} u_2^{(2)} + \dots,$$
 (C18)

where  $\Lambda = \lambda \beta_1$ . Here,  $u_0^{(2)}$  is the leading-order solution obtained above and the higher-order terms  $u_k^{(2)}$  (k > 0) are solutions of Laplace's equation. Truncating the expansion at  $O(\Lambda^{-1})$  and inserting it into boundary condition (C3) yields

$$\frac{1}{\Lambda} \frac{\partial u_1^{(2)}}{\partial x} + \frac{\partial}{\partial y} \left( \bar{\delta}(y) \frac{\partial u_1^{(2)}}{\partial y} \right) = -\frac{\partial u_0^{(2)}}{\partial x} - \beta_1 \bar{\delta}(y), \quad x = 0,$$
(C19)

where

$$\frac{\partial u_0^{(2)}}{\partial x} = \sum_{k=0}^{\infty} d_k \alpha_k \tanh\left(\frac{\alpha_k W}{2}\right) \cos \alpha_k y \tag{C20}$$

is the stress at the fluid interface from the leading-order solution

Neglecting the  $O(\Lambda^{-1})$  term in Eq. (C19) and integrating twice yields the leading-order velocity at the fluid interface,

$$u_1^{(2)}(0,y) = a_1(\beta_1, W)\log(1 - y^2) + F_5(y, \beta_1, W) + c_0,$$
(C21)

where  $F_5$  is an analytic function that vanishes at  $y \to \pm 1$ ,  $a_1$  is given by Eq. (39), and  $c_0$  is a constant.

The logarithmic singularities seen in Eq. (C21) indicate the presence of boundary layers at  $(x,y) = (0,\pm 1)$ ; the foregoing first-order correction  $u_1^{(2)}$  describes the velocity in the outer region away from these boundary layers and the constant  $c_0$  in Eq. (C21) is obtained by matching to the boundary layer velocity.

In the boundary layer, the velocity satisfies Laplace's equation,

$$\frac{1}{\tilde{r}}\frac{\partial}{\partial \tilde{r}} \left( \tilde{r} \frac{\partial \tilde{u}_{1}^{(2)}}{\partial \tilde{r}} \right) + \frac{1}{\tilde{r}^{2}} \frac{\partial^{2} \tilde{u}_{1}^{(2)}}{\partial \theta^{2}} = 0, \tag{C22}$$

where  $(r,\theta)$  defines a local polar coordinate system centered at  $(x,y)=(0,\pm 1)$ , the channel walls corresponding to  $\theta=0$ , and the fluid interface at  $\theta=\mp(\frac{\pi}{2}-\beta_1)$ . Here, the inner variables are defined as

$$\tilde{r} = \Lambda^m r, \quad \tilde{u}_1^{(2)} = u_1^{(2)}, \tag{C23}$$

where m > 0 is assumed.

Matching between the inner and the outer velocities,

$$\lim_{\tilde{r} \to \infty} \tilde{u}_1^{(2)} \iff \lim_{r \to 0} u_1^{(2)}, \tag{C24}$$

and the form of the outer velocity imposed by boundary condition (C21) requires that the far-field form of the inner velocity is

$$\lim_{\tilde{r} \to \infty} \tilde{u}_1^{(2)} = D \,\theta(\log \tilde{r} + \tilde{c}_0), \quad D = \frac{a_1(\beta_1, W)}{\pi/2 - \beta_1}, \quad (C25)$$

where  $\tilde{c}_0$  depends on  $\beta_1$  and W and is obtained by solving the inner problem.

The exponent in Eq. (C23) is taken to be m=1 under the assumption that the first term on the left side of Eq. (C19) must be retained at O(1) in the boundary layer in order to satisfy no-slip boundary conditions at  $\tilde{r}=0$ . This is motivated by the need to balance the integral of the stresses induced by the leading-order outer velocity. Accordingly, the matching condition yields

$$c_0 = a_1(\beta_1, W)(\log \Lambda + \tilde{c}_0). \tag{C26}$$

The boundary layer problem was not solved; the constant  $\tilde{c}_0$  was instead extrapolated from numerical results. The results shown in Fig. 15 show an approximately linear dependence on  $\beta_1$  and a weak dependence on W for W > 1.

The first-order correction to the velocity in Fluid 2,  $u_1^{(2)}(x,y)$ , is then given by (13) with coefficients obtained as the inner product of  $u_1^{(2)}(0,y)$  with  $\cos \alpha_k y$ . Substituting the interfacial velocity (C21) and Eq. (C26) into (27) and (28) yields formula (35) for the critical flow rate of Fluid 1. The leading-order velocity in Fluid 2  $u_0^{(2)}$  yields  $\mathcal{Q}_{\infty}^{(2)}$  [cf.

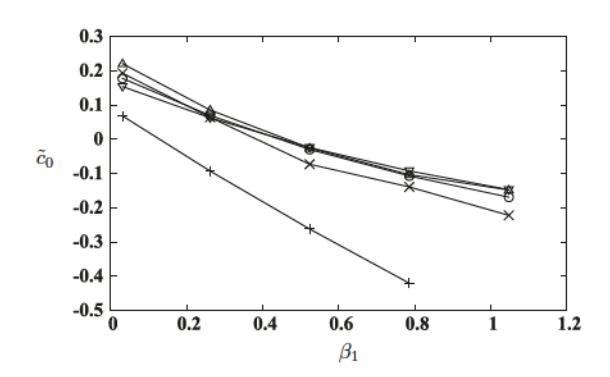


FIG. 15. Coefficient in the far-field expansion, (C25): W = 1 (crosses), W = 2 (X's), W = 3 (circles), W = 4 (upward triangles), and  $W \gg 1$  (downward triangles).

Eq. (37)] and the first-order correction  $u_1^{(2)}$  yields the  $O(\Lambda^{-1})$  component of Eq. (36).

The foregoing expansions can be extended,

$$Q_1 = \beta_1 \left[ \Lambda^{-1} \left( \frac{4a_1}{3} \log \Lambda + C_1^{(1)} \right) + \Lambda^{-2} \left( B_2^{(1)} \log \Lambda + C_2^{(1)} \right) \right], \tag{C27}$$

$$Q_2' = Q_{\infty}^{(2)} + \Lambda^{-1} (B_1^{(2)} \log \Lambda + C_1^{(2)}) + \Lambda^{-2} (B_2^{(2)} \log \Lambda + C_2^{(2)}),$$
 (C28)

where  $a_1$ ,  $C_1^{(1)}$ ,  $\mathcal{Q}_{\infty}^{(2)}$ ,  $B_1^{(2)}$ , and  $C_1^{(2)}$  correspond to Eqs. (35)–(39) and the  $O(\Lambda^{-2})$  terms were obtained by numerical extrapolation. Here, all coefficients depend on  $\beta_1$  and W.

#### APPENDIX D: WIDE-CHANNEL APPROXIMATION

Here, results are presented for critical flow rates in wide microchannels,  $W \gg 1$ . Numerical values are provided for a range of viscosity ratios  $\lambda$  and several values of the contact angle  $\beta_1$ , as indicated, in files Q1Data.txt and Q2Data.txt of the Supplemental Material [23]; file Q1Data.txt contains critical values of  $\lambda Q_1$  and file Q2Data.txt contains the corresponding critical values of  $Q_2''$  defined by

$$Q_2(\lambda, \beta_1, W) = \frac{4}{3}W - Q_2''(\lambda, \beta_1),$$
 (D1)

where

$$Q_2''(\lambda, \beta_1) = Q_2'(\lambda, \beta_1) + Q_e, \quad Q_e = 0.840332,$$
 (D2)

and  $Q_2$  is the total volume flow rate of the continuous-phase fluid. Here,  $Q_e$  takes account of edge effects in the channel and  $Q_2'$  [defined by Eq. (5)] takes account of the reduced flow due

to the presence of the dispersed phase. The results presented in Fig. 9 indicate that the wide-channel approximation is accurate for W > 3.

## 1. Limiting flow rates at low- and high-viscosity ratios

The limiting cases of low- and high-viscosity-ratios for wide channels are presented here; nonwetting and partially wetting dispersed-phase fluids are considered separately.

## a. Nonwetting dispersed-phase fluid

The limiting behavior of a nonwetting dispersed phase is presented in Sec. IVA and Appendix B. For  $W \gg 1$ , the limiting flow rates for low- and high-viscosity ratios, (29)–(32), reduce to

$$Q_1 = \frac{\pi}{8\lambda} + 1.022, \quad \lambda \ll 1,$$
 (D3)

$$Q_2'' = 1.658 + 0.5772 \,\lambda, \quad \lambda \ll 1,$$
 (D4)

and

$$Q_1 = 2.678(\log \lambda - 1.584)\lambda^{-1}, \quad \lambda \gg 1,$$
 (D5)

$$Q_2'' = 2.919 - 1.889(\log \lambda - 1.003)\lambda^{-1}, \quad \lambda \gg 1.$$
 (D6)

#### b. Partially wetting dispersed-phase fluid

The limiting behavior of a partially wetting dispersed phase is presented in Sec. IV B and Appendix C. For  $W \gg 1$ , the limiting flow rates, (33)–(36), reduce to

$$Q_1 = \frac{8}{15}\beta_1 - 0.3545\,\beta_1^2(\lambda - 1) + \frac{8}{105}\beta_1^3\lambda^{-1}, \quad \lambda\beta_1 \ll 1,$$
 (D7)

$$Q_2'' = \frac{4}{15}\beta_1(\lambda + 1) + Q_e, \quad \lambda\beta_1 \ll 1,$$
 (D8)

and

$$Q_1 = \lambda^{-1} (Q_{\infty}^{(1)} \log \lambda \beta_1 + C_1^{(1)}), \quad \lambda \beta_1 \gg 1,$$
 (D9)

$$Q_2'' = \frac{8}{15}\beta_1 + 2Q_e - (\lambda\beta_1)^{-1} (B_1^{(2)} \log \lambda\beta_1 + C_1^{(2)}),$$
  
  $\lambda\beta_1 \gg 1,$  (D10)

where

$$Q_{\infty}^{(1)} = \frac{4}{9}\beta_1 + 0.724, \quad B_1^{(2)} = 1.447\beta_1 + 4.713, \quad (D11)$$

$$C_1^{(1)} \approx -0.45 \,\beta_1 - 0.13, \quad C_1^{(2)} \approx -0.54 \,\beta_1 - 0.29. \quad (D12)$$

The values given in Eq. (D12) were obtained from a best fit of the numerical results presented in Fig. 6 corresponding to  $W \gg 1$ .

<sup>[1]</sup> C.-X. Zhao and A. Middleberg, Chem. Eng. Sci. 66, 1394 (2011).

<sup>[2]</sup> P. Garstecki, M. Fuerstman, H. Stone, and G. Whitesides, Lab Chip. 6, 437 (2006).

<sup>[3]</sup> S. L. Anna, N. Bontoux, and H. A. Stone, Appl. Phys. Lett. 82, 364 (2003).

<sup>[4]</sup> C. N. Baroud, F. Gallaire, and R. Dangla, Lab Chip. 10, 2032 (2010).

- [5] P. Guillot, P. Panizza, J.-B. Salmon, M. Joanicot, A. Colin, C.-H. Bruneau, and T. Colin, Langmuir 22, 6438 (2006).
- [6] S. Gupta, W. S. Wang, and S. A. Vanapalli, Biomicrofluidics 10, 043402 (2016).
- [7] J. Wehking, M. Gabany, L. Chew, and R. Kumar, Microfluid Nanofluid 16, 441 (2014).
- [8] S. L. Anna, Annu. Rev. Fluid Mech. 48, 285 (2016).
- [9] W. Lee, L. M. Walker, and S. L. Anna, Phys. Fluids 21, 032103 (2009).
- [10] R. Shah, H. C. Shum, A. Rowat, D. Lee, J. Agresti, A. Utada, L.-Y. Chu, J.-W. Kim, A. Fernández-Nieves, C. Martinez, and D. Weitz, Mater. Today 11, 18 (2008).
- [11] J. Lim, O. Caen, J. Vrignon, M. Konrad, V. Taly, and J.-C. Baret, Biomicrofluidics 9, 034101 (2015).
- [12] V. Sibillo, G. Pasquariello, M. Simeone, V. Cristini, and S. Guido, Phys. Rev. Lett. 97, 054502 (2006).
- [13] Y. Renardy, Rheol. Acta 46, 521 (2007).
- [14] P. Janssen, P. Anderson, and M. Loewenberg, Phys. Fluids 22, 042002 (2010).

- [15] K. J. Humphry, A. Ajdari, A. Fernández-Nieves, H. A. Stone, and D. A. Weitz, Phys. Rev. E 79, 056310 (2009).
- [16] P. Guillot, A. Colin, and A. Ajdari, Phys. Rev. E 78, 016307 (2008).
- [17] M. Zagnoni, J. Anderson, and J. M. Cooper, Langmuir 26, 9416 (2010).
- [18] P. Guillot and A. Colin, Phys. Rev. E 72, 066301 (2005).
- [19] C. Roberts, R. Rao, M. Loewenberg, C. Brooks, P. Galambos, A. Grillet, and M. Nemer, Lab Chip. 12, 1540 (2012).
- [20] J. D. Tice, A. D. Lyon, and R. F. Ismagilov, Anal. Chim Acta 507, 73 (2004).
- [21] S. Vanapalli and M. Nekouei, private communication.
- [22] A. M. Gañán Calvo and P. Riesco-Chueca, J. Fluid Mech. 553, 75 (2006).
- [23] See Supplemental Material at http://link.aps.org/supplemental/ 10.1103/PhysRevE.95.063103 for the numerical data required for the wide-channel approximation.